View Article Online
View Journal

# Dalton Transactions

An international journal of inorganic chemistry

## Accepted Manuscript

This article can be cited before page numbers have been issued, to do this please use: C. Peng, M. Xu, J. Li and W. Xie, *Dalton Trans.*, 2026, DOI: 10.1039/D6DT00401F.




ROYAL SOCIETY OF CHEMISTRY

rsc.li/dalton

View Article Online
DOI: 10.1039/D6DT00401F

# Beyond Layer Stacking: Molecular $Ru_2O_9$ Dimer Correlations in Pressure-Synthesized $Ba_3NbRu_2O_9$

Cheng Peng[1], Mingyu Xu[1], Jie Li[2], Weiwei Xie[1*]

1. Department of Chemistry, Michigan State University, East Lansing, MI, 48824 USA
2. Department of Earth and Environmental Sciences, University of Michigan, Ann Arbor, MI, 48109 USA

* Corresponding Author: Weiwei Xie (xieweiwe@msu.edu)





## *Abstract*

Ruthenium-based oxides featuring face-sharing octahedra provide a powerful chemical platform for tuning correlated electronic states through direct metal-metal interactions and valence control. Here we report the high-pressure, high-temperature synthesis and comprehensive characterization of $Ba_3NbRu_2O_9$, a previously unreported 6H-type hexagonal perovskite. Single-crystal and powder X-ray diffraction measurements confirm a fully ordered structure composed of face-sharing $Ru_2O_9$ dimers separated by corner-sharing $NbO_6$ octahedra, crystallizing in the $P6_3/mmc$ space group. Charge balance analysis reveals an unusually low mixed $Ru^{3+}/Ru^{4+}$ oxidation state (nominal $Ru^{3.5+}$), representing a reduced Ru valence realized within the $Ba_3MRu_2O_9$ family. Magnetic susceptibility measurements show Curie-Weiss behavior at high temperatures with an effective magnetic moment of 2.39 $\mu_B$ per formula unit and a negative Curie-Weiss temperature, indicating predominant antiferromagnetic interactions. Below ~15 K, a bifurcation between zero-field-cooled and field-cooled susceptibilities emerges, while the absence of a frequency-dependent shift in AC susceptibility and the lack of a λ-type anomaly in specific heat down to 1.8 K indicate a frozen spin state with short-range correlations rather than long-range magnetic order or a canonical spin-glass transition. Electrical transport measurements reveal a broad resistivity maximum near 35 K followed by a low-temperature upturn and pronounced positive magnetoresistance. Remarkably, the temperature dependence of resistance closely resembles that of the nine-layer $BaRuO_3$ polytype, despite the structural similarity of $Ba_3NbRu_2O_9$ to the four-layer phase. These results demonstrate that the electronic and magnetic properties of $Ba_3NbRu_2O_9$ are governed primarily by the molecular

View Article Online
DOI: 10.1039/D6DT00401F

electronic state of the $Ru_2O_9$ dimers rather than by crystallographic stacking alone, underscoring the central role of dimer-based correlations in low-valence ruthenates.

View Article Online
DOI: 10.1039/D6DT00401F





## Introduction

Ruthenium-based oxides have attracted sustained interest because the extended 4*d* orbitals of Ru and their strong hybridization with oxygen give rise to rich electronic behavior that often defies simple ionic descriptions. In barium ruthenates, substantial Ru-O covalency frequently invalidates strict integer oxidation-state assignments, leading instead to fractional valence states and itinerant or correlated electronic behavior.[1] When combined with face-sharing $RuO_6$ octahedra, this electronic flexibility enables direct Ru-Ru interactions and the formation of structural motifs such as dimers, trimers, and extended chains, whose electronic and magnetic properties are highly sensitive to cluster connectivity and Ru-Ru bonding. Layered $BaRuO_3$ polytypes provide a prototypical example of this structure-property interplay. The four-layer (4H) form, composed of $RuO_6$ dimers, behaves as a correlated metal, whereas the nine-layer (9R) polytype, containing linear chains of face-sharing trimers, exhibits a low-temperature resistivity upturn.[2] These contrasting behaviors within the same chemical composition demonstrate that subtle changes in Ru-Ru connectivity and cluster topology can dramatically reshape the low-energy electronic landscape of ruthenium oxides. Within this broader context, the hexagonal perovskite family $Ba_3MRu_2O_9$ offers a particularly versatile platform for systematically tuning Ru valence and dimer-based electronic states. These compounds crystallize in a 6H-type structure consisting of face-sharing $Ru_2O_9$ dimers separated by corner-sharing $MO_6$ octahedra, with the formal Ru oxidation state determined by the valence of the M-site cation. When M is tetravalent (e.g., Pr, Tb, Ce),[3] Ru commonly adopts integer oxidation states such as Ru (IV), while divalent M-site substitutions (e.g., Co, Ni) stabilize Ru (V).[4–6] In systems containing odd-valent cations, including rare-earth and alkali metals, charge balance naturally leads to mixed-valent Ru states and enhanced tunability of magnetic and electronic behavior. For example, rare-earth members $Ba_3RE(III)Ru_2O_9$ typically host mixed Ru (IV/V) dimers,[7,8] whereas hydroxide-melt synthesis of Li- or Na-containing analogues stabilizes higher Ru (V/VI) oxidation states.[9]

Importantly, systematic trends reveal that decreasing the average Ru oxidation state shortens the Ru-Ru distance and strengthens intradimer interactions, promoting molecular-orbital-derived electronic states and unconventional magnetic responses. In contrast, higher-valent compounds with longer Ru-Ru separations approach the limit of weakly interacting spin-only

View Article Online
DOI: 10.1039/D6DT00401F

moments.[10,11] These observations establish $Ba_3MRu_2O_9$ as a chemically tunable framework in which modest changes in valence and bonding can substantially alter emergent properties.

While hydroxide melts provide highly oxidizing conditions that stabilize elevated Ru oxidation states, comparatively little attention has been devoted to accessing the opposite regime of unusually reduced Ru valence within this structural family. High-pressure synthesis offers a complementary strategy by stabilizing dense frameworks capable of accommodating larger, more weakly oxidized cations and promoting shorter metal-metal contacts. Here we report the high-pressure, high-temperature synthesis and characterization of $Ba_3NbRu_2O_9$, a previously unreported 6H-type hexagonal perovskite containing mixed $Ru^{3+}/Ru^{4+}$ (nominal $Ru^{3.5+}$), representing the lowest Ru oxidation state realized to date within the $Ba_3MRu_2O_9$ family. This compound provides a new opportunity to examine how reduced valence and enhanced Ru-Ru interactions govern dimer-based electronic and magnetic behavior in 4*d* transition-metal oxides.

View Article Online
DOI: 10.1039/D6DT00401F





## Experimental Section

### Synthesis of $Ba_3NbRu_2O_9$.

**Precursor Preparation:** The ambient-pressure precursor $Ba_4NbRu_3O_{12}$ was prepared by conventional solid-state reaction using $BaCO_3$, $RuO_2$, $Nb_2O_5$, and Ru powders (Alfa Aesar, 99.99%). [12] Initially, $Ba_5Ru_2O_{12}$ was synthesized by heating a stoichiometric mixture of $BaCO_3$ and $RuO_2$ in air at 1000 °C for 12 h. The resulting $Ba_5Ru_2O_{12}$ was then thoroughly mixed with $RuO_2$, $Nb_2O_5$, and Ru metal powder in the appropriate stoichiometric ratio. The mixture was heated in air in alumina crucibles at 1000 °C for 12 h, reground, pelletized, and subsequently annealed at 1100 °C for 12 h and 1300 °C for an additional 12 h to obtain phase-pure $Ba_4NbRu_3O_{12}$.

**High-Pressure High-Temperature Transformation:** Polycrystalline $Ba_3NbRu_2O_9$ was obtained by transforming the $Ba_4NbRu_3O_{12}$ precursor under high-pressure and high-temperature conditions. The precursor powder was sealed in a Pt capsule, inserted into an alumina sleeve, and compressed using a Walker-type multi-anvil press.[13] The pressure assembly consisted of a Ceramacast 646 octahedral pressure medium, a Re heater, and Toshiba Tungaloy tungsten-carbide anvils.[14] The sample was compressed to 7 GPa at room temperature over 24 h, heated to 1350 °C, and held at that temperature for 3 h. The sample was then quenched to room temperature before slow decompression to ambient pressure. The resulting $Ba_3NbRu_2O_9$ product was stable in air.

**Crystal Structure Determination:** Single-crystal X-ray diffraction (SCXRD) was performed to determine the crystal structure. Small single-crystalline grains suitable for SCXRD were identified within the bulk high-pressure product, mechanically extracted under an optical microscope and selected based on their diffraction quality. The selected crystal ($0.051 \times 0.018 \times 0.017$ mm$^3$) was mounted on a nylon loop with Paratone oil and measured at ambient conditions using a Rigaku XtaLAB Synergy Dualflex diffractometer equipped with a Hypix detector and a microfocus Mo Kα radiation source ($\lambda = 0.71073$ Å, 50 kV, 1 mA). Data were collected using ω scans, with optimal strategies generated by CrysAlisPro (Rigaku OD, version 1.171.42.101a, 2023). Data reduction included Lorentz and polarization corrections. Absorption corrections were applied using numerical Gaussian integration over a multifaceted crystal model,[15] followed by empirical spherical harmonics scaling (SCALE3 ABSPACK).[16] The structure was solved and refined using the SHELXTL software package.[17,18] Note that single crystals obtained from high-pressure

View Article Online
DOI: 10.1039/D6DT00401F

synthesis are typically very small and may exhibit internal strain, lattice defects, or mosaicity introduced during synthesis, quenching, or decompression. These factors can affect the consistency of equivalent reflections and contribute to an elevated $R_{int}$ and residual electron-density features. Despite these limitations, the refinement converged to a chemically reasonable structural model.

**Powder X-ray Diffraction and Phase Analysis:** Phase purity of the bulk sample was verified by powder X-ray diffraction (PXRD). Crystals were ground into a fine powder and mounted on a zero-background single-crystal silicon holder. PXRD data were collected at room temperature using a Rigaku MiniFlex II diffractometer (Bragg-Brentano geometry, Cu Kα radiation, λ = 1.5406 Å) over a 2θ range of 5°-100° with a step size of 0.01° and a dwell time of 3 s per step. Rietveld refinement was performed using the GSAS-II software suite.[19]

**Physical Property Measurements:** Temperature- and field-dependent magnetic measurements were carried out using a Quantum Design Magnetic Property Measurement System (MPMS) over the temperature range 1.8-300 K in applied fields up to 9 T. AC susceptibility measurements were performed at frequencies between 10 and 1000 Hz. Electrical resistivity was measured using a standard four-probe configuration on pelletized samples with platinum contacts in a Quantum Design Physical Property Measurement System (PPMS) from 1.8 to 300 K. Specific heat measurements were conducted using a PPMS DynaCool equipped with a heat-capacity option over the temperature range 1.8-150 K.

View Article Online
DOI: 10.1039/D6DT00401F



## Results and Discussion

The high-pressure phase of $Ba_3NbRu_2O_9$ crystallizes in the hexagonal $P6_3/mmc$ space group, as determined by single-crystal X-ray diffraction (SCXRD) (crystallographic details are provided in **Tables S1** and **S2**). The bulk phase purity and structural consistency were verified by powder X-ray diffraction (PXRD) using the SCXRD-derived model. Rietveld refinement of the PXRD data (**Figure 1**) yields a final weighted R-factor (wR) of 10.14% based on 7391 observations, which is considered satisfactory given the limited sample quantity and the internal strain commonly associated with metastable phases synthesized under high pressure. The refined PXRD profile is in good agreement with the SCXRD structural model, confirming the phase purity and crystallographic assignment. A two-phase Rietveld refinement suggests the presence of a minor $BaRuO_3$ impurity (~7.7 wt%), while $Ba_3NbRu_2O_9$ remains the dominant phase. The presence of a minor $BaRuO_3$ impurity does not affect the overall magnetic and transport behavior. Structurally, $Ba_3NbRu_2O_9$ consists of face-sharing $RuO_6$ octahedral pairs forming $Ru_2O_9$ dimers arranged in a honeycomb network within the *ab*-plane. These dimers alternate along the *c*-axis with corner-sharing $NbO_6$ octahedra, generating the characteristic 6H-type hexagonal perovskite framework.[20] A related structural motif has been reported for the iridium analogue.[21] However, whereas partial Nb/Ir site mixing (~9:1 occupancy ratio) is observed in that system, no detectable cation disorder is found in $Ba_3NbRu_2O_9$.

View Article Online
DOI: 10.1039/D6DT00401F



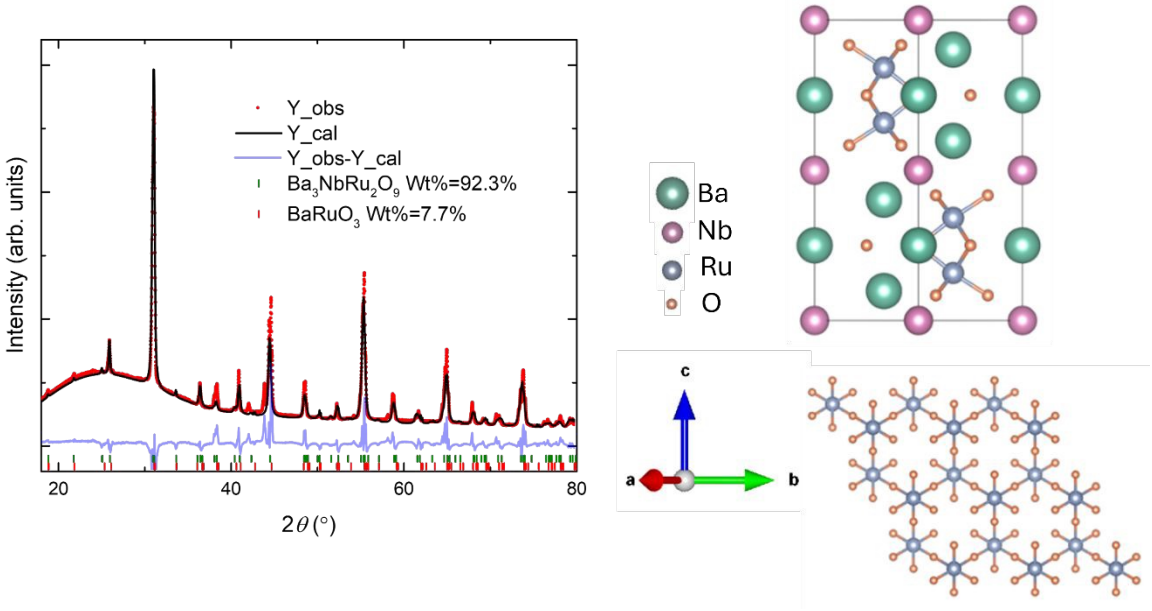


**Figure 1. Powder X-ray diffraction (PXRD) pattern and crystal structure of high-pressure $Ba_3NbRu_2O_9$.** The experimental data (red circles) are fitted by Rietveld refinement (black solid line), and the blue curve represents the difference between the observed and calculated profiles. Bragg reflection positions for $Ba_3NbRu_2O_9$ and $BaRuO_3$ are indicated by green and red tick marks, respectively. The structural model highlights the arrangement of face-sharing $RuO_6$ octahedra forming $Ru_2O_9$ dimers within the 6H-type hexagonal perovskite framework.

Bond-valence-sum (BVS) calculations [22] based on the refined structural parameters yield oxidation states of +4.81 for Nb and +3.74 for Ru, in good agreement with the nominal charge balance and supporting a mixed $Ru^{3+}/Ru^{4+}$ configuration. It is important to note that BVS values reflect spatially (and potentially temporally) averaged oxidation states over the crystallographic Ru site and therefore may not fully capture the local electronic configurations within individual $Ru_2O_9$ dimers. This averaged structural picture is consistent with the magnetic behavior discussed below, where the susceptibility can be understood as a statistical average over multiple dimer spin configurations associated with distinct local electronic states. Among reported 6H-type perovskites of the general formula $Ba_3MRu_2O_9$, ruthenium typically adopts significantly higher oxidation states. For example, $Ba_3M^{1+}Ru^{5.5+}{}_2O_9$ (M = Li, Na)[9] stabilizes $Ru^{5.5+}$, $Ba_3M^{2+}Ru^{5+}{}_2O_9$ (M = Ca, Co, Ni, Zn)[4,5,23,24] hosts $Ru^{5+}$, $Ba_3M^{3+}Ru^{4.5+}{}_2O_9$ (M = Y, In, La, Nd, Sm, Eu, Lu)[7,8] contains $Ru^{4.5+}$, $Ba_3M^{4+}Ru^{4+}{}_2O_9$ (M = Ce, Pr, Tb)[3] stabilizes $Ru^{4+}$. To our knowledge, no member of this structural family has previously exhibited a Ru oxidation state approaching +3.5. To further contextualize this unusually reduced valence, we compared the average Ru-O bond distances

View Article Online
DOI: 10.1039/D6DT00401F



within the $Ru_2O_9$ dimers to those reported for other $Ba_3MRu_2O_9$ compounds (**Figure 2**). As expected, the average Ru-O bond length systematically increases with decreasing Ru oxidation state, consistent with reduced Coulombic attraction between the less positively charged Ru cations and surrounding oxide anions. In contrast, the intradimer Ru-Ru separation exhibits the opposite trend, decreasing as the Ru oxidation state is lowered (**Figure S1**), reflecting enhanced direct metal-metal interaction in the more reduced regime.

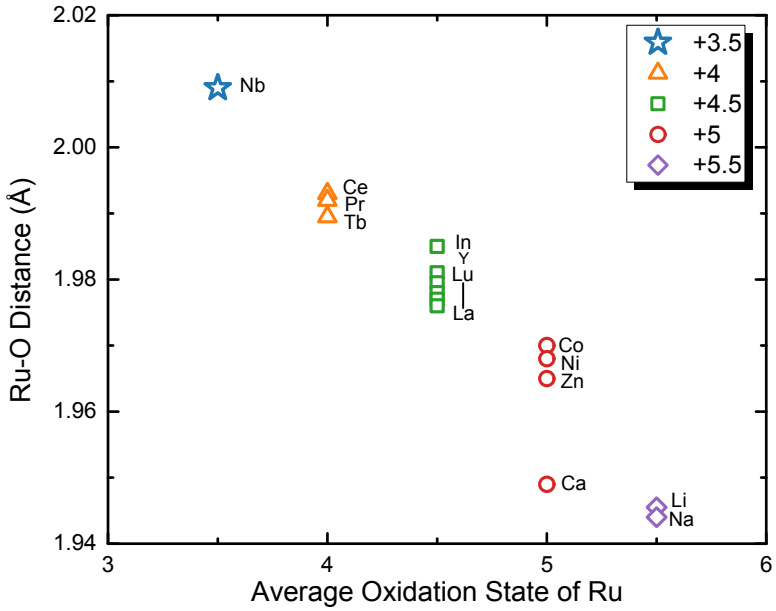


**Figure 2.** Dependence of the average Ru-O bond distance within the $Ru_2O_9$ dimers on the formal Ru oxidation state in $Ba_3MRu_2O_9$ compounds. Comparative data are included for M = Li, Na ($Ru^{5.5+}$);[9] M = Ca, Co, Ni, Zn ($Ru^{5+}$);[4,5,23,24] M = Y, In, La, Nd, Sm, Eu, Lu ($Ru^{4.5+}$);[7,8] and M = Ce, Pr, Tb ($Ru^{4+}$).[3] Literature sources are provided in the main text.

To probe the magnetic behavior of the high-pressure phase, temperature-dependent magnetic susceptibility measurements were performed under both zero-field-cooled warming (ZFCW) and field-cooled (FC) protocols (**Figure 3**). Between 15 and 300 K, the ZFCW and FC curves overlap under applied magnetic fields ranging from 100 Oe to 50 kOe, indicating the absence of magnetic irreversibility in this temperature range. In contrast, a clear bifurcation between the ZFCW and FC susceptibilities emerges below approximately 15 K under an applied field of 10 kOe (left inset, **Figure 3**), signaling the onset of a frozen spin state. The right inset shows the temperature derivative of $\chi T$, where $\chi$ was calculated as M/H under the applied magnetic field.[25] A pronounced anomaly in this derivative at low temperatures further supports the development of spin freezing.

View Article Online
DOI: 10.1039/D6DT00401F



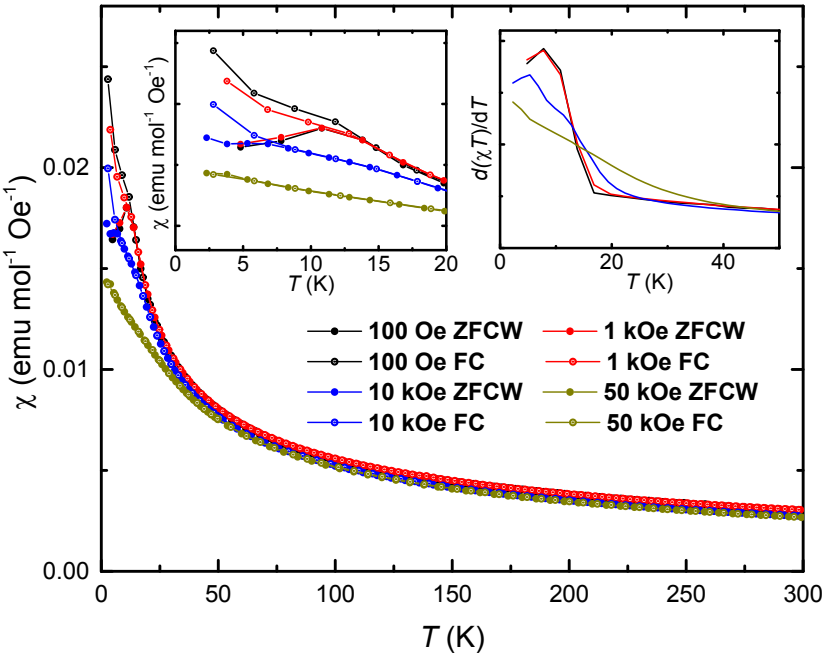


**Figure 3.** Temperature-dependent magnetic susceptibility of high-pressure $Ba_3NbRu_2O_9$ measured under zero-field-cooled warming (ZFCW) and field-cooled (FC) protocols at various applied magnetic fields. The left inset highlights the low-temperature region, showing the bifurcation between ZFCW and FC curves. The right inset displays the temperature derivative $d(\chi T)/dT$.

The observed magnetic response is consistent with frustrated magnetism accompanied by short-range correlations. Although a bifurcation between ZFC and FC susceptibilities is evident in the DC measurements, the absence of a clear frequency-dependent shift in the AC susceptibility peak (**Figure S2**) argues against a canonical spin-glass transition.[26] Notably, a spin-glass ground state has been reported in $Ba_3TiRu_2O_9$ and attributed to significant Ti/Ru site disorder.[27] In contrast, $Ba_3NbRu_2O_9$ exhibits a chemically ordered structure without detectable mixing yet displays similar low-temperature spin freezing. This comparison suggests that the freezing behavior in the present compound is intrinsic to the $Ru_2O_9$ dimer network rather than arising from chemical disorder. The high-temperature magnetic susceptibility (100-300 K) measured under an applied field of 100 Oe is well described by the modified Curie-Weiss expression,

$$\chi = \chi_0 + \frac{C}{T-\theta_{cw}} \quad (1)$$

as shown in **Figure 4**, where $\chi_0$ represents the temperature-independent contribution, $C$ is the Curie constant, and $\theta_{cw}$ is the paramagnetic Curie temperature. Least-squares fitting yields $\chi_0 = 1.04 \times$

View Article Online
DOI: 10.1039/D6DT00401F



$10^{-3}$ emu $mol^{-1}$ $Oe^{-1}$ and $\theta_{cw}$ = -63.2 K, the negative value indicating dominant antiferromagnetic interdimer interactions. The extracted effective magnetic moment, $\mu_{eff}$ = 2.39 $\mu_B$/f.u., lies between the Hund's-rule limits expected for S = 1/2 (1.73 $\mu_B$/f.u.) and S = 3/2 (3.87 $\mu_B$/f.u.). Given the possible presence of a minor impurity phase, the absolute value of $\mu_{eff}$ may contain some uncertainty because the magnetization was normalized using the total sample mass. Nevertheless, the intermediate value is consistent with a dimer-based magnetic state influenced by mixed valence and electronic correlations.

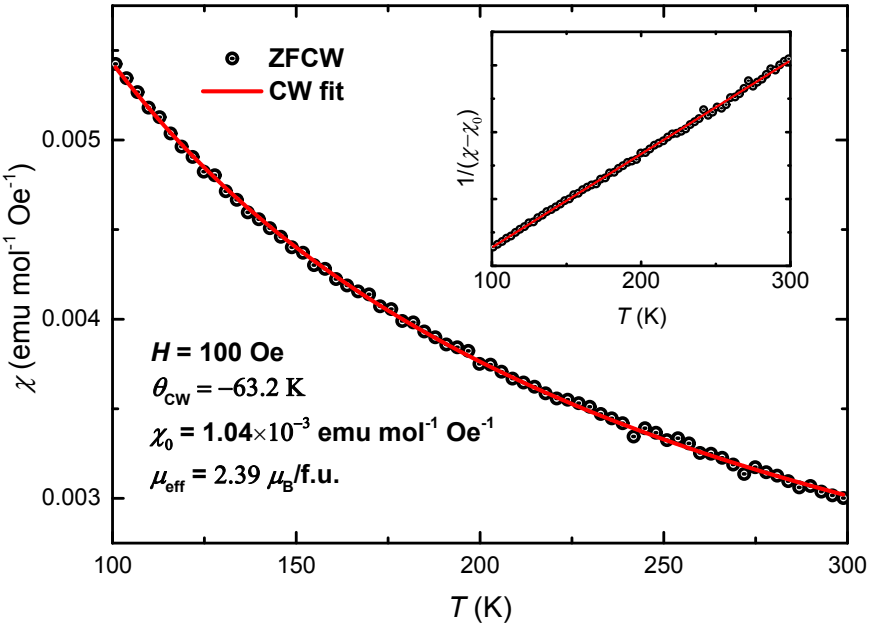


**Figure 4.** Curie-Weiss fitting of the temperature-dependent magnetic susceptibility measured under zero-field-cooled warming (ZFCW) conditions in an applied field of 100 Oe over the temperature range 100-300 K. The inset shows the linear dependence of $1/(\chi-\chi_0)$ versus temperature used to extract the Curie constant and paramagnetic Curie temperature.

Because $Nb^{5+}$ is nonmagnetic, the magnetic response of $Ba_3NbRu_2O_9$ originates predominantly from the $Ru_2O_9$ dimers. Owing to the short Ru-Ru separation, the relevant magnetic degrees of freedom are more appropriately described at the dimer level rather than in terms of isolated Ru ions. Within a molecular-orbital framework for a mixed-valent Ru-Ru dimer, multiple total spin configurations (e.g., S = 1/2 or S = 3/2; **Figure S3**) may be stabilized depending on the competition among intradimer hopping, Hund's exchange, on-site Coulomb repulsion, and spin-orbit coupling.[28,29] The temperature dependence of the $\chi$T product provides insight into this dimer-based

View Article Online
DOI: 10.1039/D6DT00401F



magnetism. Notably, $\chi T$ does not exhibit clear saturation up to 300 K and already exceeds the Curie-limit value expected for an isolated S = 1/2 moment (0.375 emu K mol$^{-1}$ Oe$^{-1}$; **Figure S4**), thereby excluding a simple S = 1/2 high-temperature limit. This behavior indicates that the extracted $\mu_{eff}$ reflects an apparent moment within an intermediate-temperature regime, where electronic correlations remain significant, rather than a fully uncorrelated paramagnetic limit. Consequently, a higher-spin dimer configuration (e.g., S = 3/2) cannot be excluded within the accessible temperature window. Importantly, $Ba_3NbRu_2O_9$ contains an unusually low mixed $Ru^{3+}/Ru^{4+}$ valence distributed over a single crystallographically unique Ru site. This implies electronic (valence) disorder at the microscopic level within the Ru-Ru dimers, leading to a distribution of local electronic configurations and spin states. The measured magnetic susceptibility therefore represents a thermal and configurational average over multiple dimer spin configurations on the experimental timescale, consistent with the structurally averaged mixed-valence state inferred from the BVS analysis.

Field-dependent magnetization measurements further support this picture (**Figure 5**). At temperatures below 3 K, the magnetization exhibits a small hysteresis loop without saturation up to 5 T, consistent with short-range magnetic correlations and frozen spin components. In contrast, at temperatures above 50 K, the magnetization varies linearly with applied field, indicative of a paramagnetic state consistent with the Curie-Weiss analysis.

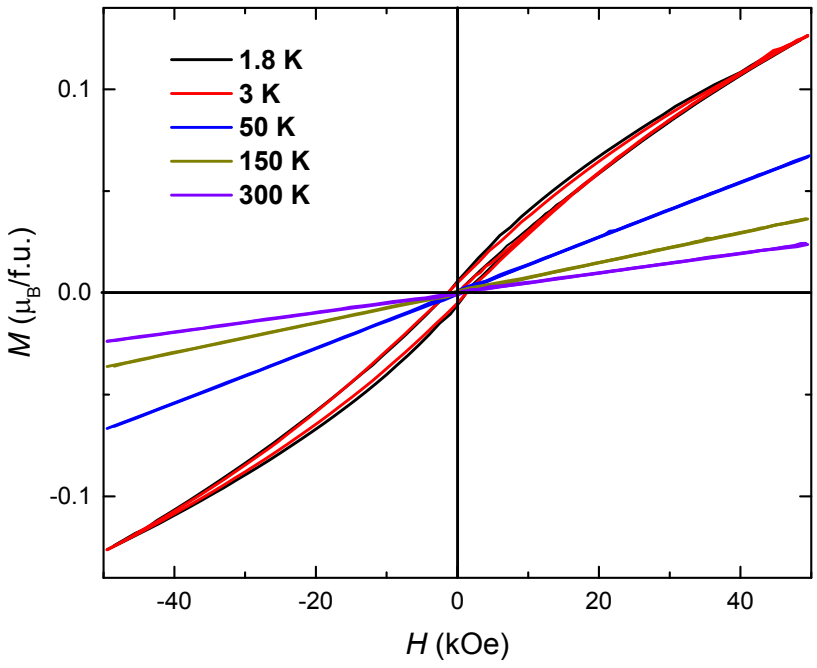

View Article Online
DOI: 10.1039/D6DT00401F

**Figure 5. Field-dependent magnetization of high-pressure $Ba_3NbRu_2O_9$ measured up to 5 T at selected temperatures.** The low-temperature curves exhibit a small hysteresis without magnetic saturation, while higher-temperature data show linear field dependence characteristic of paramagnetic behavior.

The temperature-dependent specific heat of high-pressure $Ba_3NbRu_2O_9$ was measured under applied magnetic fields of 0 and 9 T over the range 1.8-150 K (**Figure 6*a***). A subtle deviation near 15 K is observed, consistent with the development of short-range magnetic correlations. However, no λ-type anomaly is detected down to 1.8 K, indicating the absence of long-range magnetic ordering within the measured temperature window. At elevated temperatures, the specific heat is dominated by lattice (phonon) contributions. To quantify the phonon background, the high-temperature data (30-150 K) were fitted using harmonic lattice models. Neither a single Debye model (eq 2) nor a single Einstein model (eq 3) alone provides an adequate description of the experimental data, necessitating a more comprehensive treatment of the lattice contribution.

$$C_{\mathrm{D}} = 9nR\left(\frac{T}{\theta_D}\right)^3 \int_0^{\theta_D/T} \frac{x^4 e^x}{(e^x-1)^2}\,dx \quad (2)$$

$$\mathrm{C}_E = 3nR\left(\frac{\theta_E}{T}\right)^2 e^{\theta_E/T}(e^{\theta_E/T}-1)^{-2} \quad (3)$$

where $n$ is the number of atoms per formula unit, $R$ is the gas constant, $\theta_D$ is the Debye temperature and $\theta_E$ is the Einstein temperature.

The specific heat data in the temperature range 30-150 K are well described by a combined two-Debye-Einstein model (eq 4), as shown in **Figure 6*b***. The fitting yields characteristic temperatures of $\theta_{\mathrm{D1}}$ = 399(81) K, $\theta_{\mathrm{D2}}$ = 208(14) K, $\theta_{\mathrm{E}}$ = 579(43) K, with corresponding oscillator strengths $s_{\mathrm{D1}}$ = 5.0(5), $s_{\mathrm{D2}}$ = 3.2(9), and $s_{\mathrm{E}}$ = 5.3(1.2). The total lattice heat capacity is expressed as

$$C = 9s_{D1}R\left(\frac{T}{\theta_{D1}}\right)^3 \int_0^{\theta_{D1}/T} \frac{x^4 e^x}{(e^x-1)^2}\,dx + 9s_{D2}R\left(\frac{T}{\theta_{D2}}\right)^3 \int_0^{\theta_{D2}/T} \frac{x^4 e^x}{(e^x-1)^2}\,dx + 3s_E R\left(\frac{\theta_E}{T}\right)^2 e^{\theta_E/T} (e^{\theta_E/T}-1)^{-2} \quad (4)$$

The resulting phonon model converges to a high-temperature heat capacity of 42(3)$R$, which is in good agreement with the Dulong-Petit limit of 3$nR$ for $n$ = 15 atoms per formula unit. This consistency confirms that the model provides a reasonable description of the phonon-dominated

View Article Online
DOI: 10.1039/D6DT00401F

regime. Due to the absence of a nonmagnetic structural analogue, however, the magnetic contribution to the specific heat cannot be quantitatively isolated.

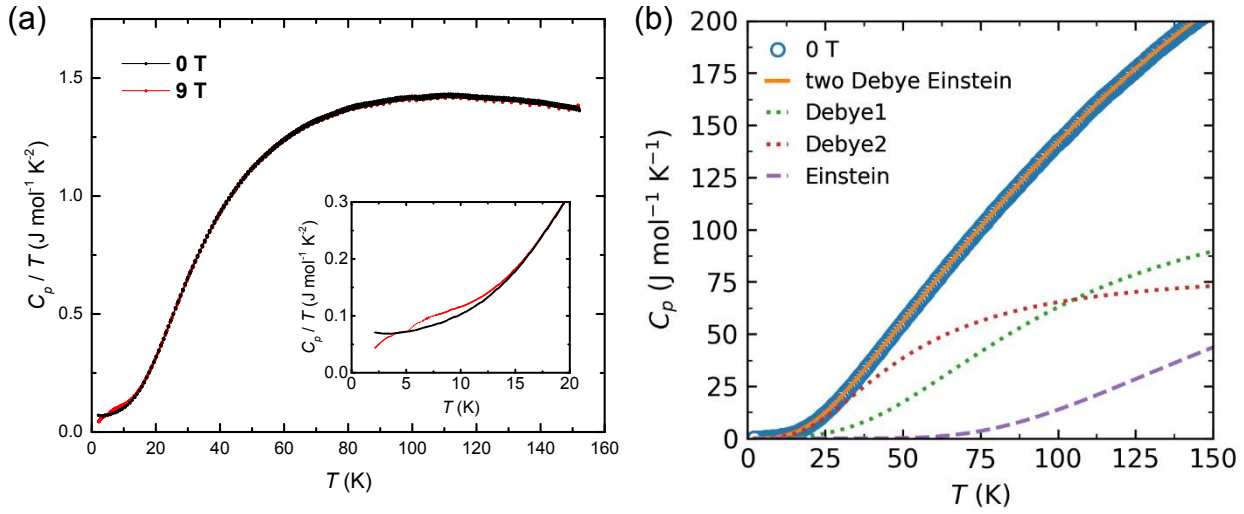


**Figure 6. (*a*)** Temperature dependence of $C_p/T$ for high-pressure $Ba_3NbRu_2O_9$ measured under applied magnetic fields of 0 T (black) and 9 T (red). **(*b*)** Fit of the specific heat data using a combined two-Debye–Einstein model (orange solid line). The green, red, and purple dotted curves represent the 1st Debye, 2nd Debye, and Einstein contributions, respectively.

As shown in **Figure S5**, the low-temperature specific heat in the range 1.8-10 K follows a linear dependence of $C_p/T$ versus $T^2$, which is well described by

$$C_p/T = \gamma + \beta T^2 \quad (5)$$

where $\gamma = 0.0626(3)$ J mol$^{-1}$ K$^{-2}$ and $\beta = 3.83(6) \times 10^{-4}$ J mol$^{-1}$ K$^{-4}$ represent the electronic and lattice contributions, respectively. The finite $\gamma$ term indicates the presence of additional low-energy excitations beyond conventional acoustic phonons, consistent with correlated electronic or magnetic degrees of freedom. From the $\beta$ coefficient, the Debye temperature can be estimated using

$$\theta_D = \left(\frac{12\pi^4}{5\beta n R}\right)^{1/3} \quad (6)$$

yielding $\theta_D$ = 424 K. This value is comparable to the characteristic Debye temperatures extracted from the high-temperature phonon model, demonstrating internal consistency between the low- and high-temperature lattice analyses.

View Article Online
DOI: 10.1039/D6DT00401F



The electrical transport data were normalized to their respective values at 300 K, where the absolute resistance ranges from approximately 0.25 to 0.28 Ω. The temperature dependence of the normalized resistance under applied magnetic fields up to 9 T is shown in Figure 7 over the range 1.8-300 K. A broad resistivity maximum appears near 35 K, followed by an upturn upon further cooling, Indicating a crossover from a relatively metallic regime to a weakly localized transport state. The magnitude of this maximum increases systematically with applied magnetic field, indicating positive magnetoresistance. Notably, this crossover closely resembles that reported for the nine-layer (9L) $BaRuO_3$ polytype, rather than the four-layer (4L) phase, despite the structural analogy of $Ba_3NbRu_2O_9$ to the 4L stacking motif. This comparison suggests that transport in $Ba_3NbRu_2O_9$ is governed primarily by the molecular electronic structure of the $Ru_2O_9$ dimers, particularly mixed valence and correlated spin or charge fluctuations, rather than by the crystallographic stacking sequence alone. Further electronic structure calculations would help clarify the microscopic origin of this transport behavior.

The resemblance to the transport behavior of 9L-$BaRuO_3$ further indicates that the dominant energy scale for charge transport is set by intra-dimer electronic interactions. In the present system, the short Ru-Ru distance and mixed-valence configuration favor the formation of molecular orbitals within the $Ru_2O_9$ dimers, including partially occupied antibonding states. This electronic structure can lead to enhanced carrier scattering from low-energy spin and charge fluctuations localized on the dimers. Within this framework, the broad resistivity maximum is interpreted as a crossover from a high-temperature incoherent transport regime to a low-temperature state dominated by local electronic correlations and fluctuation-driven scattering, rather than a simple gap opening or polaronic freezing. This interpretation is consistent with the absence of a sharp anomaly in the specific heat and the presence of short-range magnetic correlations inferred from susceptibility measurements.

View Article Online
DOI: 10.1039/D6DT00401F



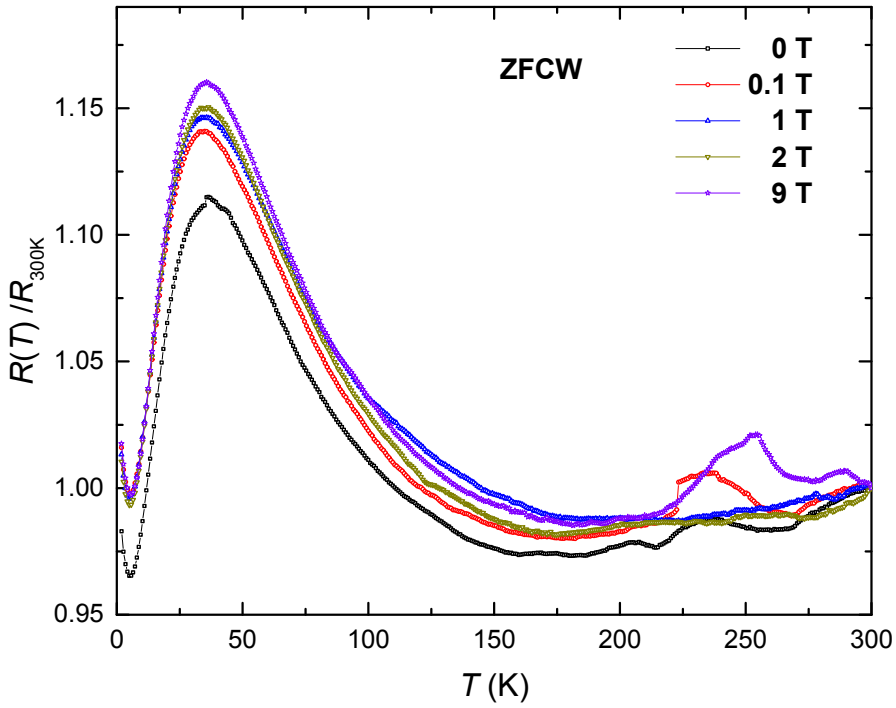


**Figure 7. Temperature dependence of the normalized electrical resistance of $Ba_3NbRu_2O_9$ under applied magnetic fields up to 9 T.** The resistance is scaled to its respective value at 300 K for each field.

## Conclusion

In summary, we have synthesized and characterized $Ba_3NbRu_2O_9$, a new member of the $Ba_3MRu_2O_9$ family stabilized under high-pressure and high-temperature conditions. Structural analysis confirms a fully ordered 6H-type hexagonal perovskite framework composed of face-sharing $Ru_2O_9$ dimers separated by $NbO_6$ octahedra, with bond-valence analysis indicating an unusually low mixed $Ru^{3+}/Ru^{4+}$ configuration corresponding to a nominal oxidation state of +3.5, the most reduced Ru valence reported to date within this structural family. Magnetic measurements reveal Curie-Weiss behavior with dominant antiferromagnetic interactions and the emergence of a frozen spin state with short-range correlations below ~15 K, in the absence of long-range magnetic order or a canonical spin-glass transition. The extracted effective moment reflects an intermediate-temperature average over multiple dimer spin configurations, consistent with a molecular-orbital description of mixed-valent Ru-Ru dimers governed by competing hopping and

View Article Online
DOI: 10.1039/D6DT00401F





correlation effects, while specific heat data further support this picture by showing no sharp thermodynamic anomaly but evidence of additional low-energy excitations. Electrical transport measurements place $Ba_3NbRu_2O_9$ in a weakly localized regime characterized by a broad resistivity maximum, low-temperature upturn, and positive magnetoresistance. The similarity of its transport behavior to that of nine-layer $BaRuO_3$, despite structural analogy to the four-layer polytype, demonstrates that crystallographic stacking alone does not dictate the electronic response; rather, the molecular electronic structure of the $Ru_2O_9$ dimers plays the central role in governing correlated behavior. These results establish $Ba_3NbRu_2O_9$ as a new chemically accessible platform for investigating low-valence dimer-based correlations in 4d transition-metal oxides.

**Supporting Information:** The crystal structure and refinement of $Ba_3NbRu_2O_9$; Atomic coordinates and equivalent isotropic atomic displacement parameters; Variation of the average Ru–Ru bond distance with Ru oxidation state; Temperature-dependent AC magnetic susceptibilities at various frequencies; Energy-level and spin occupation diagram for a hybridized $Ru^{3.5+}$-$Ru^{3.5+}$ dimer; The temperature dependence of $\chi T$; Low-temperature heat capacity plotted as $C_p/T$ vs. $T^2$. (DOS)

## Acknowledgement

The work at Michigan State University is supported by NSF-DMR-2422361. The work at the University of Michigan was supported by NSF-DMR-2422362.

## References

(1) Cava, R. J.; Xie, W. Are Barium Ruthenates Interesting? *Chem. Mater.* **2024**, *36* (11), 5325–5330. https://doi.org/10.1021/acs.chemmater.4c00699.

(2) Rijssenbeek, J. T.; Jin, R.; Zadorozhny, Yu.; Liu, Y.; Batlogg, B.; Cava, R. J. Electrical and Magnetic Properties of the Two Crystallographic Forms of BaRuO 3. *Phys. Rev. B* **1999**, *59* (7), 4561–4564. https://doi.org/10.1103/PhysRevB.59.4561.

(3) Doi, Y.; Wakeshima, M.; Hinatsu, Y.; Tobo, A.; Ohoyama, K.; Yamaguchi, Y. Crystal Structures and Magnetic Properties of the 6H-Perovskites $Ba_3LnRu_2O_9$ (Ln = Ce, Pr, and Tb). *J. Mater. Chem.* **2001**, *11* (12), 3135–3140. https://doi.org/10.1039/B105134M.

View Article Online
DOI: 10.1039/D6DT00401F



(4) Lightfoot, P.; Battle, P. D. The Crystal and Magnetic Structures of $Ba_3NiRu_2O_9$, $Ba_3CoRu_2O_9$, and $Ba_3ZnRu_2O_9$. *J. Solid State Chem.* **1990**, *89* (1), 174–183. https://doi.org/10.1016/0022-4596(90)90309-L.

(5) Rijssenbeek, J. T.; Huang, Q.; Erwin, R. W.; Zandbergen, H. W.; Cava, R. J. The Crystal Structure of $Ba_3CuRu_2O_9$ and Comparison to $Ba_3MRu_2O_9$ (M = In, Co, Ni, and Fe). *J. Solid State Chem.* **1999**, *146* (1), 65–72. https://doi.org/10.1006/jssc.1999.8309.

(6) Zhou, H. D.; Kiswandhi, A.; Barlas, Y.; Brooks, J. S.; Siegrist, T.; Li, G.; Balicas, L.; Cheng, J. G.; Rivadulla, F. Orbital, Charge, and Spin Couplings in $Ru_2^{5+}O_9$ Dimers of $Ba_3CoRu_2O_9$. *Phys. Rev. B* **2012**, *85* (4), 041201. https://doi.org/10.1103/PhysRevB.85.041201.

(7) Doi, Y.; Hinatsu, Y.; Shimojo, Y.; Ishii, Y. Crystal Structure and Magnetic Properties of 6H-Perovskite $Ba_3NdRu_2O_9$. *J. Solid State Chem.* **2001**, *161* (1), 113–120. https://doi.org/10.1006/jssc.2001.9296.

(8) Doi, Y.; Matsuhira, K.; Hinatsu, Y. Crystal Structures and Magnetic Properties of 6H-Perovskites $Ba_3MRu_2O_9$ (M = Y, In, La, Sm, Eu, and Lu). *J. Solid State Chem.* **2002**, *165* (2), 317–323. https://doi.org/10.1006/jssc.2002.9538.

(9) Stitzer, K. E.; Smith, M. D.; Gemmill, W. R.; zur Loye, H.-C. Novel Mixed-Valent (V/VI) Triple Perovskite Ruthenates: Observation of a Complex Low-Temperature Structural and Magnetic Transition. *J. Am. Chem. Soc.* **2002**, *124* (46), 13877–13885. https://doi.org/10.1021/ja0271781.

(10) Miiller, W.; Avdeev, M.; Zhou, Q.; Studer, A. J.; Kennedy, B. J.; Kearley, G. J.; Ling, C. D. Spin-Gap Opening Accompanied by a Strong Magnetoelastic Response in the S = 1 Magnetic Dimer System $Ba_3BiRu_2O_9$. *Phys. Rev. B* **2011**, *84* (22), 220406. https://doi.org/10.1103/PhysRevB.84.220406.

(11) Hayashida, S.; Gretarsson, H.; Puphal, P.; Isobe, M.; Goering, E.; Matsumoto, Y.; Nuss, J.; Takagi, H.; Hepting, M.; Keimer, B. Magnetic Ground State of the Dimer-Based Hexagonal Perovskite $Ba_3ZnRu_2O_9$. *Phys. Rev. B* **2025**, *111* (10), 104418. https://doi.org/10.1103/PhysRevB.111.104418.

(12) Nguyen, L. T.; Halloran, T.; Xie, W.; Kong, T.; Broholm, C. L.; Cava, R. J. Geometrically Frustrated Trimer-Based Mott Insulator. *Phys. Rev. Mater.* **2018**, *2* (5), 054414. https://doi.org/10.1103/PhysRevMaterials.2.054414.

(13) Li, J. Synthesis of High-Pressure Silicate Polymorphs Using Multi-Anvil Press. In *Static and Dynamic High Pressure Mineral Physics*; Walter, M. J., Fei, Y., Eds.; Cambridge University Press: Cambridge, 2022; pp 266–299. https://doi.org/10.1017/9781108806145.012.

(14) Walker, D.; Li, J. Castable Solid Pressure Media for Multianvil Devices. *Matter Radiat. Extrem.* **2020**, *5* (1), 018402. https://doi.org/10.1063/1.5129534.

View Article Online
DOI: 10.1039/D6DT00401F



(15) Parkin, S.; Moezzi, B.; Hope, H. *XABS* 2: An Empirical Absorption Correction Program. *J. Appl. Crystallogr.* **1995**, *28* (1), 53–56. https://doi.org/10.1107/S0021889894009428.

(16) Walker, N.; Stuart, D. An Empirical Method for Correcting Diffractometer Data for Absorption Effects. *Acta Crystallogr. A* **1983**, *39* (1), 158–166. https://doi.org/10.1107/S0108767383000252.

(17) Sheldrick, G. M. SHELXT – Integrated Space-Group and Crystal-Structure Determination. *Acta Crystallogr. Sect. Found. Adv.* **2015**, *71* (1), 3–8. https://doi.org/10.1107/S2053273314026370.

(18) Sheldrick, G. M. Crystal Structure Refinement with SHELXL. *Acta Crystallogr. Sect. C Struct. Chem.* **2015**, *71* (1), 3–8. https://doi.org/10.1107/S2053229614024218.

(19) Toby, B. H.; Von Dreele, R. B. GSAS-II: The Genesis of a Modern Open-Source All Purpose Crystallography Software Package. *J. Appl. Crystallogr.* **2013**, *46* (2), 544–549. https://doi.org/10.1107/S0021889813003531.

(20) Nguyen, L. T.; Cava, R. J. Hexagonal Perovskites as Quantum Materials. *Chem. Rev.* **2020**, *121* (5), 2935–2965. https://doi.org/10.1021/acs.chemrev.0c00622.

(21) Peng, C.; Xu, M.; Li, J.; Xie, W. Single-Electron Bond in Ir–Ir Dimer Stabilized under Pressure. *Inorg. Chem.* **2025**, *64* (46), 23097–23107. https://doi.org/10.1021/acs.inorgchem.5c04558.

(22) Brese, N. E.; O'Keeffe, M. Bond-Valence Parameters for Solids. *Acta Crystallogr. B* **1991**, *47* (2), 192–197. https://doi.org/10.1107/S0108768190011041.

(23) Darriet, J.; Drillon, M.; Villeneuve, G.; Hagenmuller, P. Interactions Magnétiques Dans Des Groupements Binucléaires Du Ruthénium +V. *J. Solid State Chem.* **1976**, *19* (3), 213–220. https://doi.org/10.1016/0022-4596(76)90170-5.

(24) Wilkens, J.; Müller-Buschbaum, Hk. Einkristalluntersuchung an $Ba_3CaRu_2O_9$. *J. Alloys Compd.* **1991**, *177* (2), L31–L33. https://doi.org/10.1016/0925-8388(91)90071-3.

(25) Fisher, M. E. Relation between the Specific Heat and Susceptibility of an Antiferromagnet. *Philos. Mag. J. Theor. Exp. Appl. Phys.* **1962**, *7* (82), 1731–1743. https://doi.org/10.1080/14786436208213705.

(26) Paulsen, C. C.; Williamson, S. J.; Maletta, H. Evidence for a Phase Transition in the Spin Glass $Eu_{0.4}Sr_{0.6}S$ from Dynamic Susceptibility Measurements. *Phys. Rev. Lett.* **1987**, *59* (1), 128–131. https://doi.org/10.1103/PhysRevLett.59.128.

(27) Nguyen, L. T.; Cava, R. J. A Spin Glass State in $Ba_3TiRu_2O_9$. *J. Magn. Magn. Mater.* **2019**, *476*, 334–336. https://doi.org/10.1016/j.jmmm.2018.12.087.

View Article Online
DOI: 10.1039/D6DT00401F

(28) Ziat, D.; Aczel, A. A.; Sinclair, R.; Chen, Q.; Zhou, H. D.; Williams, T. J.; Stone, M. B.; Verrier, A.; Quilliam, J. A. Frustrated Spin-½ Molecular Magnetism in the Mixed-Valence Antiferromagnets $Ba_3MRu_2O_9$ (M = In, Y, Lu). *Phys. Rev. B* **2017**, *95* (18), 184424. https://doi.org/10.1103/PhysRevB.95.184424.

(29) Chen, Q.; Verrier, A.; Ziat, D.; Clune, A. J.; Rouane, R.; Bazier-Matte, X.; Wang, G.; Calder, S.; Taddei, K. M.; Cruz, C. R. dela; Kolesnikov, A. I.; Ma, J.; Cheng, J.-G.; Liu, Z.; Quilliam, J. A.; Musfeldt, J. L.; Zhou, H. D.; Aczel, A. A. Realization of the Orbital-Selective Mott State at the Molecular Level in $Ba_3LaRu_2O_9$. *Phys. Rev. Mater.* **2020**, *4* (6), 064409. https://doi.org/10.1103/PhysRevMaterials.4.064409.

View Article Online
DOI: 10.1039/D6DT00401F

## Data Availability Statement

- Crystallographic data for $Ba_3NbRu_2O_9$ has been deposited at the CCDC under 2549437 and can be obtained from https://www.ccdc.cam.ac.uk/structures/.
- The datasets supporting this article have been uploaded as part of the supplementary information.
- Data is available from the authors upon reasonable request.